

See discussions, stats, and author profiles for this publication at: <https://www.researchgate.net/publication/303697307>

# Low-Cost, High-Resolution, Self-Powered, Miniaturized Sun Sensor For Space Applications

Conference Paper · June 2016

---

CITATION

1

READS

289

3 authors:



[Andrea Antonello](#)

University of Padova

20 PUBLICATIONS 40 CITATIONS

[SEE PROFILE](#)



[Lorenzo Olivieri](#)

University of Padova

58 PUBLICATIONS 149 CITATIONS

[SEE PROFILE](#)



[Alessandro Francesconi](#)

University of Padova

115 PUBLICATIONS 590 CITATIONS

[SEE PROFILE](#)

Some of the authors of this publication are also working on these related projects:



Project Investigation on the dynamics of tethered space tug maneuvers [View project](#)



Project Development of a low cost Sun Sensor [View project](#)

# LOW-COST, HIGH-RESOLUTION, SELF-POWERED, MINIATURIZED SUN SENSOR FOR SPACE APPLICATIONS

**Andrea Antonello<sup>1</sup>, Lorenzo Olivieri<sup>1</sup>, Alessandro Francesconi<sup>1,2</sup>**

<sup>1</sup>*CISAS G. Colombo, University of Padova, Italy;* <sup>2</sup>*DII, University of Padova, Italy*

## ABSTRACT

Among attitude determination sensors, Sun Sensors represent a simple and reliable technology employed in many space missions, allowing to determine the relative position of a body respect to the Sun measuring the incident angle of the solar radiation. A common baseline for two-axis digital Sun sensors consists in an array of active pixels arranged behind a small aperture: the position of the spot illuminated by Sun rays allows to determine the direction of the Sun.

With the advent of smaller vehicles such as cubesats and nanosats, there is the need to limit size and weight of such devices: as a trade-off, this usually results in the curtail of the performances.

Nowadays, standard off-the-shelf components for CubeSats have accuracies up to  $0.3^\circ$  with fields of view ranging from  $\pm 45^\circ$  to  $\pm 90^\circ$ , and costs of several thousands of euros.

In this paper we present a low-cost miniaturized Sun sensor based on a commercial CMOS camera. The device uses a precision pinhole aperture of  $20\ \mu\text{m}$ , with a  $7\ \text{mm}$  stand-off with the CMOS. The geometry and the design allows for a maximum resolution of less than  $0.05^\circ$ , overcoming most of the currently available commercial solutions. The nature of the technology allows for reduced size as well as limited weight.

We introduce the design, the development and the laboratory tests of the sensor. A first mathematical model was used to define the sensor geometrical layout and theoretical resolution. A more accurate model was then developed in order to take into account the geometrical deviation and deformations of the projected spot, as well as the background noise of both ground and space environment. The model, in addition, allows for the prevention of diffraction noise.

Finally, the laboratory setup is presented along with the test campaigns. The results obtained, compared with the simulations, allowed the validation of the theoretical model.

A final section is dedicated to assessing the feasibility of adding an array of solar cells on the top surface in order for the sensor to be capable of generating enough power to be autonomous.

## 1 INTRODUCTION

In the last decade the small satellites market showed a continuous increase thanks to the high interest such vehicles are creating in the space sector: thanks to their low development and

launch cost with respect to their larger counterpart, research centers, universities and enterprises can access space to perform their tests and researches.

As direct consequence, a dedicated network of small enterprises and start-ups is flourishing, to give users the possibility to procure the main standard elements for their spacecraft bus and structure. In this contest, the request of low-cost high-accuracy reliable small sensors for attitude determination is still not totally satisfied: available components are usually scaled versions of bigger sensors, with heavy requirements and high cost that are not balanced with good accuracy and precision. In particular, one of the best off-the-shelf sensors reaches an accuracy of  $0.3^\circ$  and a precision of  $0.05^\circ$ , with a size of  $40 \times 30$  mm and a weight of 25 g [1]. Sun sensors can be classified depending on their outputs: 1-D sensors are able to give a single angular information regarding the sun direction, and their measure can be performed with an analog [2] or a digital system [3-4]; their theoretical resolution can be up to  $0.07^\circ$  [4]. Complete information on the sun position can be obtained by using two 1-D elements or by implementing a 2-D sensor, usually consisting in a photo-sensible surface covered by a mask; the light rays passing through the mask and illuminating the surface can be detected to reconstruct the direction of the Sun [5-6]. In the cited case, average accuracy can be less than  $0.01^\circ$ , but with a mass of 2 kg [7].

In this framework, the University of Padova is developing a cohort of sensors to be used on cubesats and nanosats platform. To this day, relative navigation sensors have been developed [8-9], and a new sun sensor is under investigation. The idea behind the proposed device is to have a small, yet precise attitude sensor which can be placed on a cubesat with a very limited footprint. The driving philosophy behind the project is to use off-the-shelf components and custom software to obtain a reliable piece of equipment that could be feasible for a multitude of applications, from miniaturized commercial spacecraft to academic demonstrators.

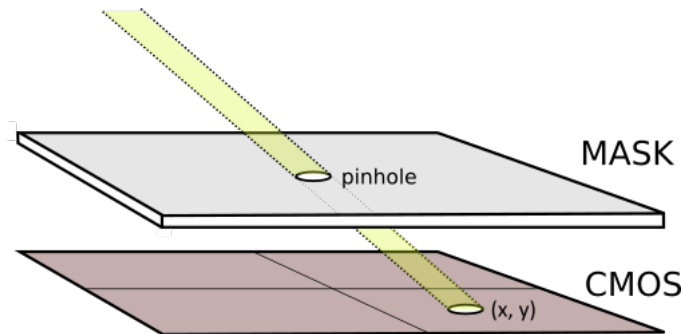


Figure 1. Sensor layout

As visible in Figure 1, the device is made up of two parts: an active pixel sensor (CMOS) and a mask. The mask presents a circular hole through which the sun can filtrate: the active pixel sensor is used as the light spot detector. By knowing the coordinates of the spot on the CMOS it is possible to use simple trigonometry to infer the azimuth and elevation angles of the Sun with respect to the CMOS plane.

In this paper, the sensor general layout and its working principle are presented, focusing on its modeling in a Matlab environment. A second part is dedicated to the description of the

experimental setup and to the data collected during its tests and calibration. In particular, the presence of diffraction patterns will be explained and the effect on the sensor accuracy will be discussed.

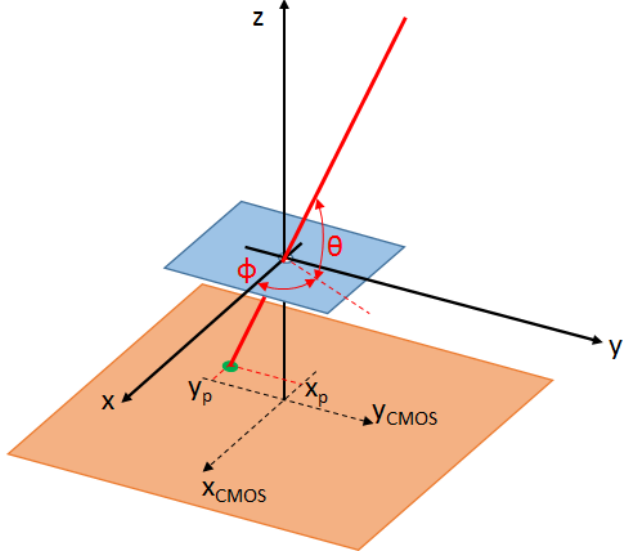


Figure 2. Sensor reference geometry: the direction to the Sun with respect to the reference plane  $xy$  is defined by azimuth  $\Phi$  and elevation  $\theta$ . The illuminated spot center coordinates is

$$x_p, y_p$$

## 2 GEOMETRICAL MODEL AND SIMULATIONS

The geometrical model of the proposed sensor is visible in Figure 2, with the reference frames on the mask (blue) and the CMOS-plane (orange). As previously mentioned, the sensor measures the direction of the Sun vector (red), i.e. the relative direction of the Sun in the field of view. This information can be represented both with azimuth and elevation angles ( $\Phi$  and  $\theta$ ) or with the related versor  $\mathbf{v} = (\cos\Phi\cos\theta, \sin\Phi\cos\theta, \sin\theta)$ . Both formulations can be derived knowing the light spot position  $(x_{CMOS}, y_{CMOS})$ , since the distance  $h$  between the mask and the CMOS is known:

$$\mathbf{v} = \frac{(x_{CMOS}, y_{CMOS}, h)}{\sqrt{x_{CMOS}^2 + y_{CMOS}^2 + h^2}} \quad (1)$$

This formulation does not involve any trigonometric function, and a unique and real solution exists for any position of the light spot on the CMOS.

By knowing the size of the CMOS and the mask mounting distance it is possible to define the sensor theoretical field of view, considering an ideal mask with negligible thickness and no diffraction. For the sensor described in this work, the two field-of-view angles  $\theta_1$  and  $\theta_2$  represented in Figure 3 are respectively of  $64.1^\circ$  and  $49.0^\circ$ .

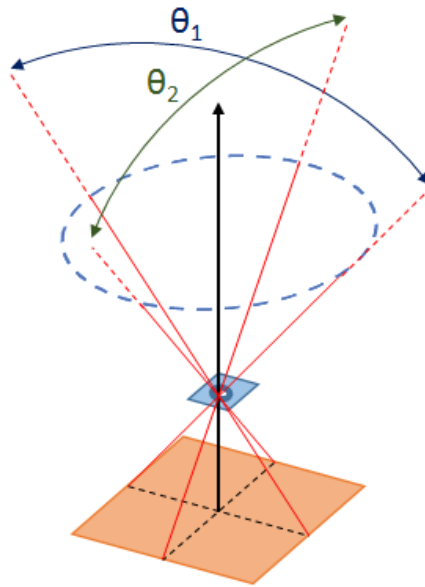


Figure 3. The sensor field of view, represented by the dashed blue ellipsoid, can be described by the two view angles  $\theta_1$  and  $\theta_2$

## 2.1 Simulations

The aforementioned geometrical description allowed for the development of three different models of increasing sophistication analyzing the sun sensor response to the incoming radiation, as reported in Figure 5. In the ideal case of a mask with no thickness, the projected light spot has the exact size and shape of the mask hole; by measuring the center of the light spot it is possible to calculate directly the Sun-direction versor.

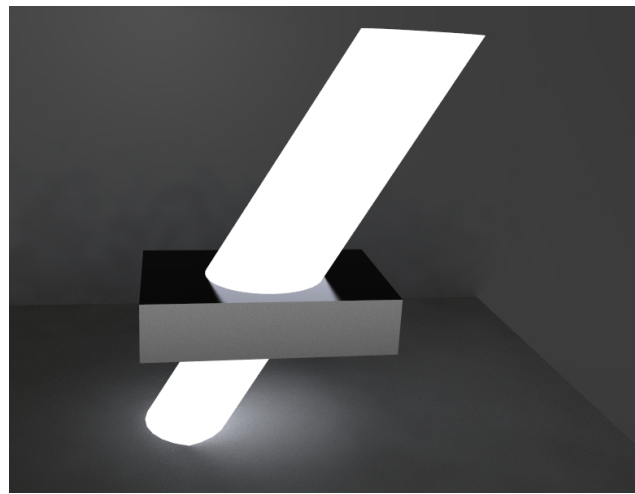


Figure 4. Simulation of the effect of mask thickness in the project light spot

As long as the mask thickness is negligible, such approximation can be acceptable.

The mask used in our device has thickness comparable to the hole diameter, so part of the incoming radiation is stopped by the mask border, modifying the shape of the light spot

detected by the CMOS (Figure 4, Figure 5: second row). Comparing the new shape with the circle from the previous model (no thickness effect), it is possible to note a translation of the light spot center. Both models have been developed by using an ideal light source, that is, a punctiform source with parallel incoming rays.

However, the Sun angular diameter is not negligible on Earth, having an incoming radiation aperture of  $\approx 0.5^\circ$ . For this reason, the third developed model adds such property to the previous efforts, yielding the results visible in the third row of Figure 5.

The spot is consistently larger than the previous one, and the center translation with respect to the first model is still visible.

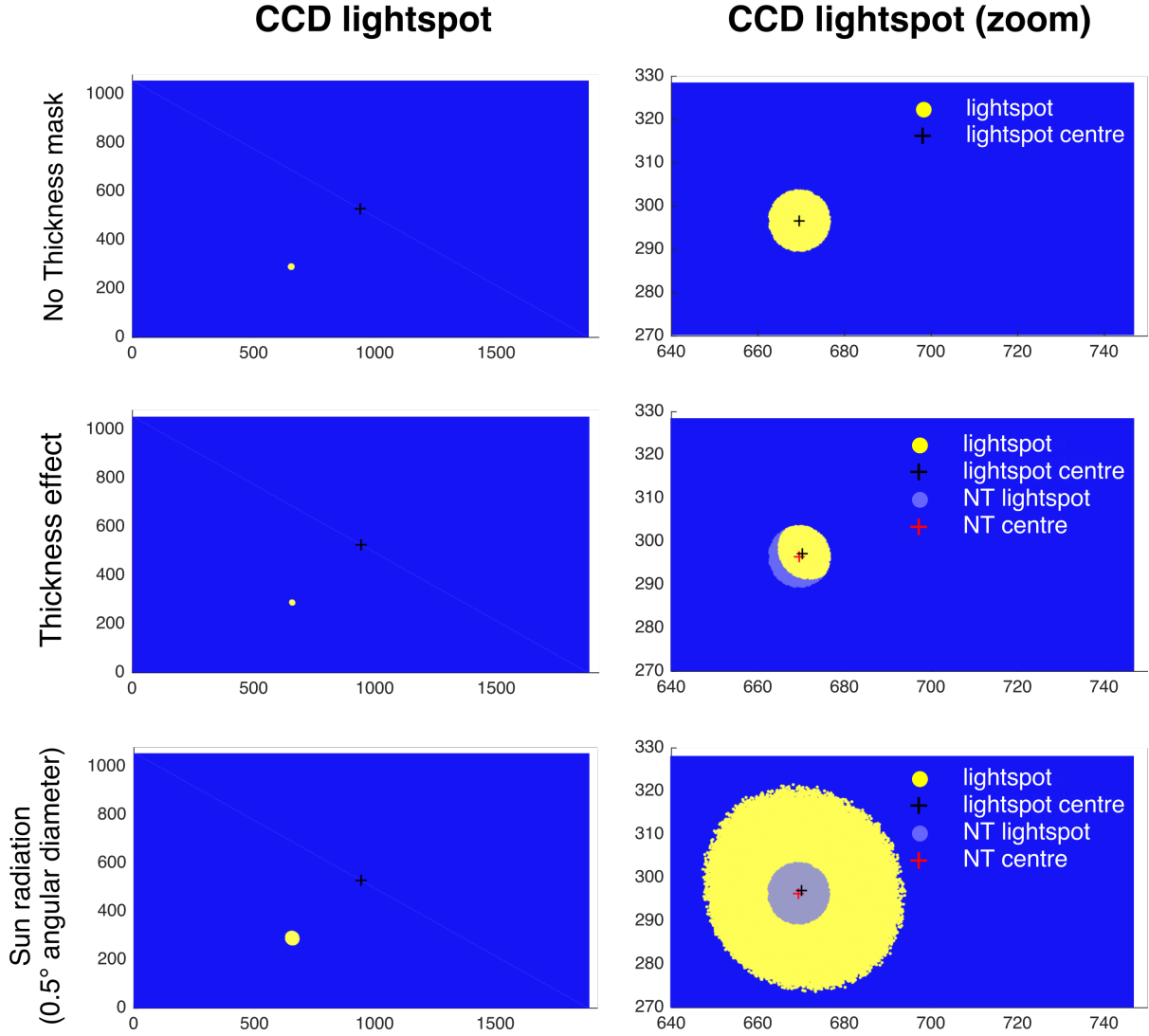


Figure 5. Sun sensor simulations, three different models: from top to down the spot projection considering (1) no mask thickness, (2) mask thickness, and (3) the effect of Sun angular diameter with respect to a punctiform origin

The center translation due to the aforementioned effects can be evaluated: the maximum bias is of about 5 pixels, which is equivalent to  $0.12^\circ$ .

The sensor software will be designed to evaluate the translation and to calculate the right orientation. This modeling can be performed by noting that the geometry of the problem allows for axialsymmetric simplifications. The piecewise equation describing the shape of the projected sunspot, in polar coordinates (further expressed in terms of azimuth and elevation angles), is:

$$f(\phi, \theta) = \begin{cases} r(\theta) - 2r(\theta)(x_0 \cos \phi + y_0 \sin \phi) + x_0^2 + y_0^2 = d^2 & R_{C0} - \frac{d}{2} < r < R_{C0} + \frac{\Delta C}{2} \\ r(\theta) - 2r(\theta)(x_1 \cos \phi + y_1 \sin \phi) + x_1^2 + y_1^2 = d^2 & R_{C1} - \frac{\Delta C}{2} < r < R_{C1} + \frac{d}{2} \end{cases} \quad (2)$$

in which:

$$r(\theta) = (t + h) \cdot \tan\left(\frac{\pi}{2} - \theta\right) \quad (3)$$

$$\Delta C = h \cdot \tan\left(\frac{\pi}{2} - \theta\right) \quad (4)$$

$$\begin{cases} R_{C0} = \sqrt{x_0^2 + y_0^2} \\ R_{C1} = \sqrt{x_1^2 + y_1^2} \end{cases} \quad (5)$$

$$\begin{cases} x_1 = \Delta C \cdot \cos(\phi + \pi) \\ y_1 = \Delta C \cdot \sin(\phi + \pi) \end{cases} \quad \begin{cases} x_0 = (t + h) \cdot \tan\left(\frac{\pi}{2} - \theta\right) \cdot \cos(\phi + \pi) \\ y_0 = (t + h) \cdot \tan\left(\frac{\pi}{2} - \theta\right) \cdot \sin(\phi + \pi) \end{cases} \quad (6)$$

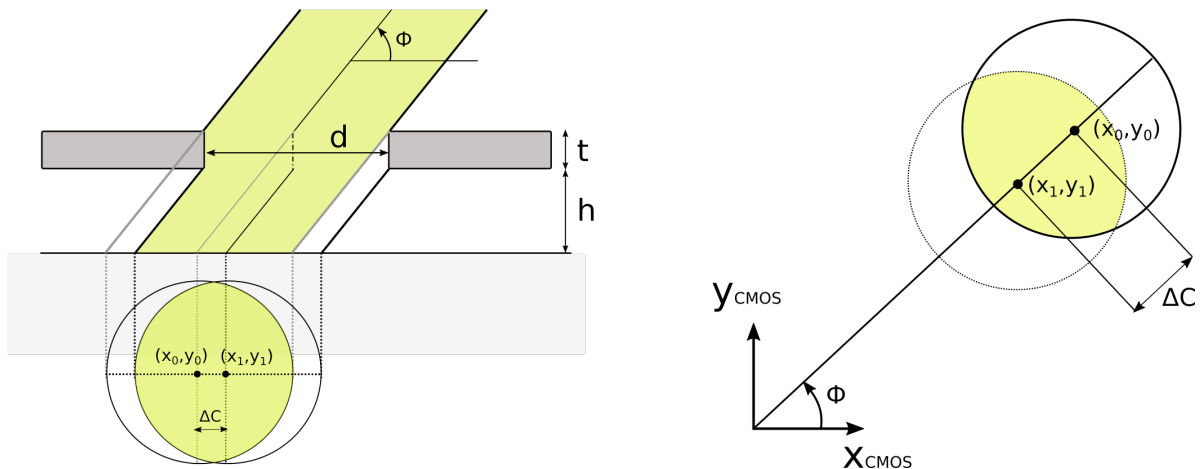


Figure 6. Schematic representation of the effects that mask thickness has in the perturbation of the projected light spot.

## 2.2 Diffraction estimation

A preliminary assessment of the effect of diffraction on the developed sensor has been performed. In fact, the utilization of a thin 20  $\mu\text{m}$  diameter circular hole could lead to diffraction effects in the involved wavelengths (in the range 500-700 nm), with the formation of an Airy Pattern; the first minimum in the pattern can be calculated with the following formula:

$$\alpha \approx 1.22 \cdot \frac{\lambda}{d} \quad (8)$$

with  $\alpha$  being the angle at which the first minimum occur,  $\lambda$  the radiation wavelength and  $D$  the hole diameter. In this case,  $\alpha$  is in the range  $1.75^\circ$ - $2.45^\circ$ , meaning that the Airy Disk is larger than the projected spot.

However, as visible in Figure 7, the intensity of the Airy Disk decrease with the distance from the center: by thresholding the image at 85% radiation intensity it is possible to reduce the Airy Disk aperture to  $0.34^\circ$ - $0.48^\circ$ , thus avoiding disturbances in the light-spot center determination.

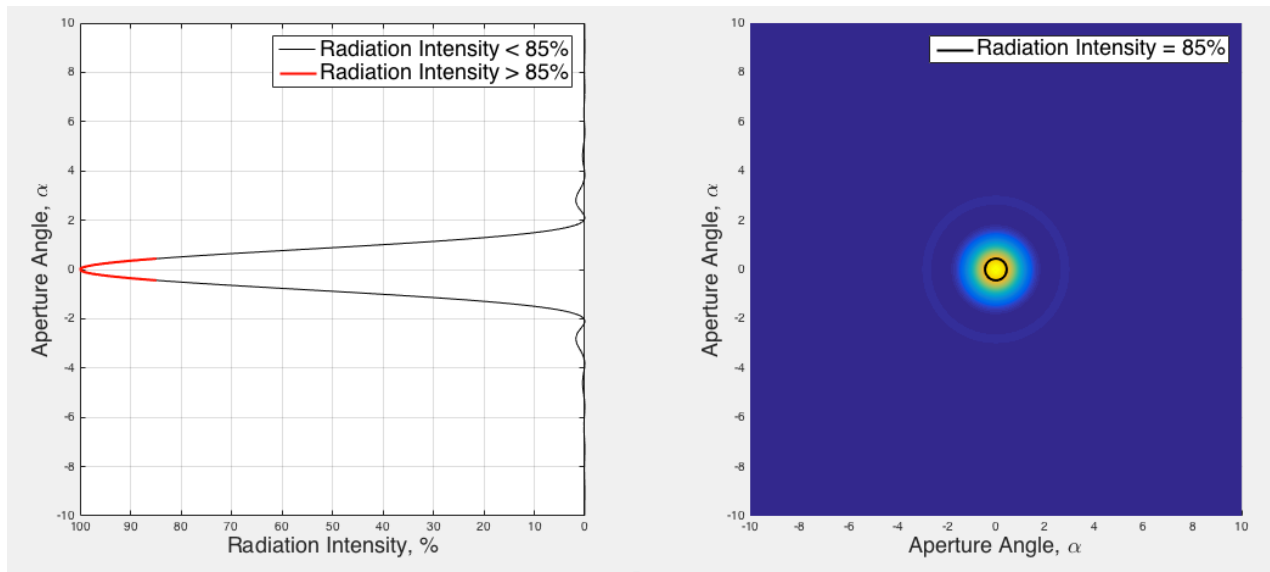


Figure 7. Diffraction effect from the 20  $\mu\text{m}$  mask ( $\lambda=600$  nm; by filtering the signal at 85% of the peak intensity it is possible to delete most of the diffracted radiation)

## 2.3 Resolution

The theoretical sensor resolution is limited by the pixel size, which in the case under analysis is 1.4  $\mu\text{m}$  x 1.4  $\mu\text{m}$ . In order to get an insight of the performances of our system, we simulated the resolution across the entire CMOS surface.

The formula representing the angular accuracy of camera module, expressed in polar coordinates, is:

$$\alpha(r, \theta) = \alpha(r) \doteq \tan^{-1} \left( \frac{r}{t+h} \right) - \tan^{-1} \left( \frac{r - px}{t+h} \right) \quad (9)$$

Where  $h$  is the CMOS-mask distance,  $r$  is the distance from the pinhole center,  $px$  is the side-size of a pixel,  $t$  is the thickness of the mask.

Figure 8 depicts the resolutions expressed in terms of arcminutes. It can be seen that the maximum resolution uncertainty occurs in the proximity of the center of the sensor (under the hypothesis that this is collinear with the pinhole center). The maximum value is 1.6 arcmins, which, with the current setup, corresponds to a maximum resolution uncertainty of  $0.026^\circ$ . This value could be eventually lowered by decreasing the distance between the sensor and the CMOS and by using a sensor with a smaller pixel size.

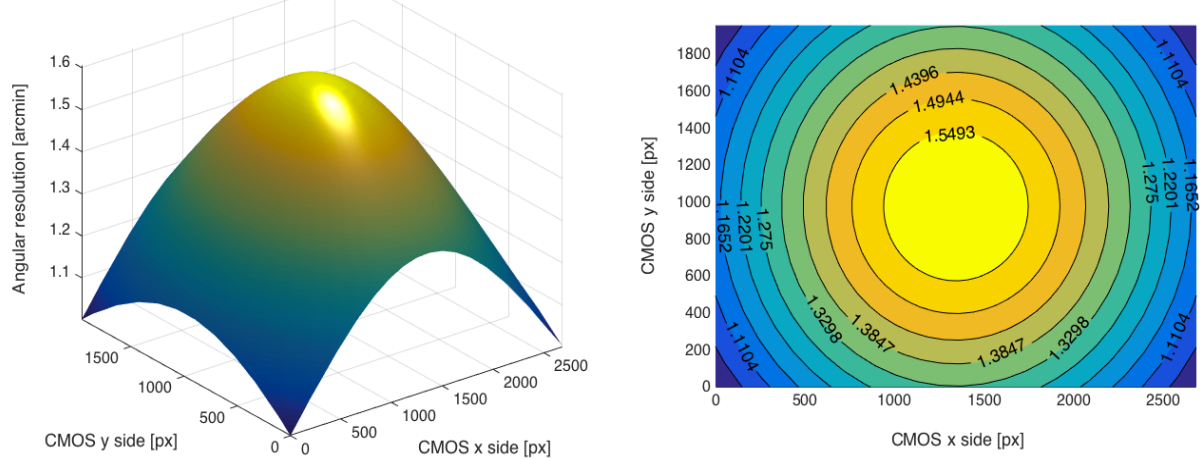


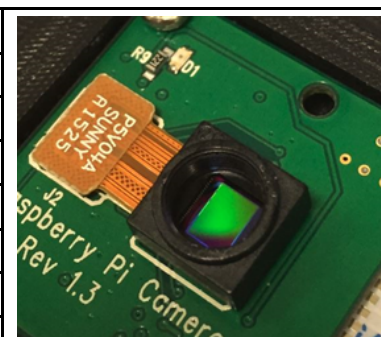
Figure 8. Resolution characteristics of the CMOS sensor under analysis. Three dimensional plot and contour line plot.

### 3 EXPERIMENTAL SETUP

When it comes to active pixels sensors, two choices are available: CCDs and CMOS. Nowadays, CMOS represent the commercial standard, they are less expensive and have a limited power consumption when compared to CCDs. On the other hand, CCDs have better SNR profiles and are much simpler to handle and to interface with the acquisition hardware. For this sensor, we chose a commercial camera module based on CMOS technology (Raspberry Pi Camera Module<sup>©</sup>), whose characteristics (in terms of pixel size and footprint) appeared to be the most suited to our application:

Tab 1: Raspberry Pi Camera Module<sup>©</sup> characteristics

Raspberry Pi Camera Module <sup>©</sup>	
<b>Size</b>	25 x 24 x 9 mm
<b>Weight</b>	3g
<b>Still resolution</b>	5 Megapixels
<b>Sensor resolution</b>	2592 x 1944 pixels
<b>Sensor image area</b>	3.76 x 2.74 mm
<b>Pixel size</b>	1.4 $\mu$ m x 1.4 $\mu$ m
<b>Net price</b>	<\$25
<b>S/N ratio</b>	36 dB



The experimental setup is composed by:

- acquisition PC (2.4 GHz i5, 8GB RAM)
- interfacing board (Raspberry PI 2 Model B<sup>©</sup>)
- CMOS sensor (Raspberry Pi Camera Module<sup>©</sup>)
- pinhole aperture (Edmund Optics<sup>®</sup>)
- enclosing hardware (3D printed)

Which are schematically represented in Figure 9:

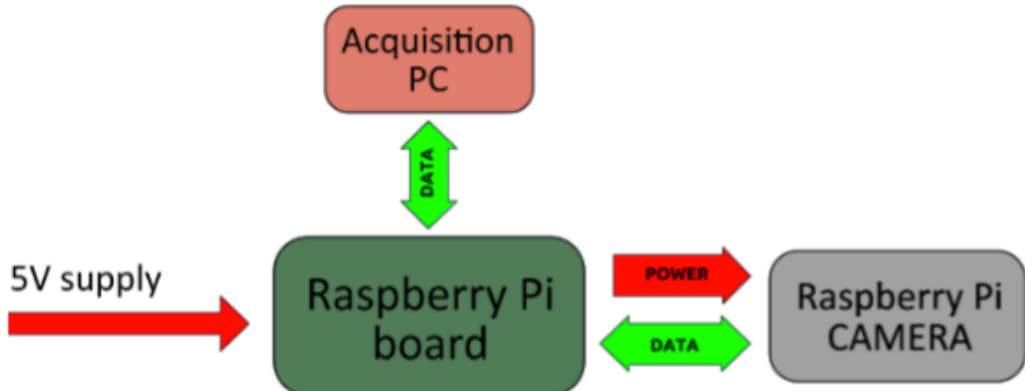


Figure 9: Experimental setup

This type of camera, however, is commercially distributed with a mounted lens. In order for the device to be used in this paper, the optics was removed, leaving an exposed CMOS. Then, by using a 3D-printed adapter, the pinhole was placed on top of the CMOS, at a distance of 3 mm from the active surface.

The pinhole, which is a commercial device manufactured by Edmund Optics<sup>®</sup>, consists of a thin metal film (25  $\mu$ m) on which a 20  $\mu$ m diameter circular hole has been etched (Figure 10). The circularity and size of the hole have been verified through SEM microscopy.

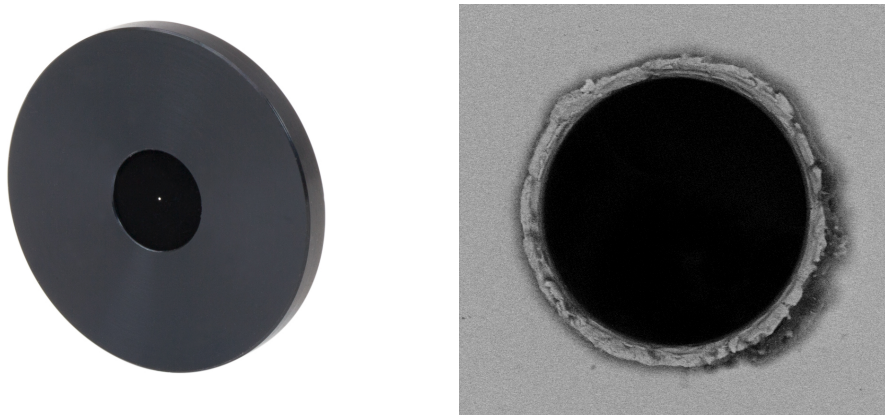


Figure 10. Pinhole aperture in mounted position and under SEM microscopy to verify circularity and diameter

### 3.1 Precision

In order to obtain the metrological characteristics of the system, several tests were performed. The precision of the sensor has been obtained experimentally in order to get an insight of the reproducibility. To simulate in a laboratory environment the emittance of the Sun, we used an array of high power white LEDs arranged in a square pattern, whose emittance was computed to be close to  $1300 \text{ W/m}^2$  in the area invested by the light. By using such a device, placed 2 meters from the pinhole aperture, perpendicular to the CMOS-plane, we took 300 measures to investigate the accuracy of the sensor (Figure 11): the scatter plot has been offset to the mean value of the acquisition and 90%, 95% and 99% confidence ellipses have been plotted.

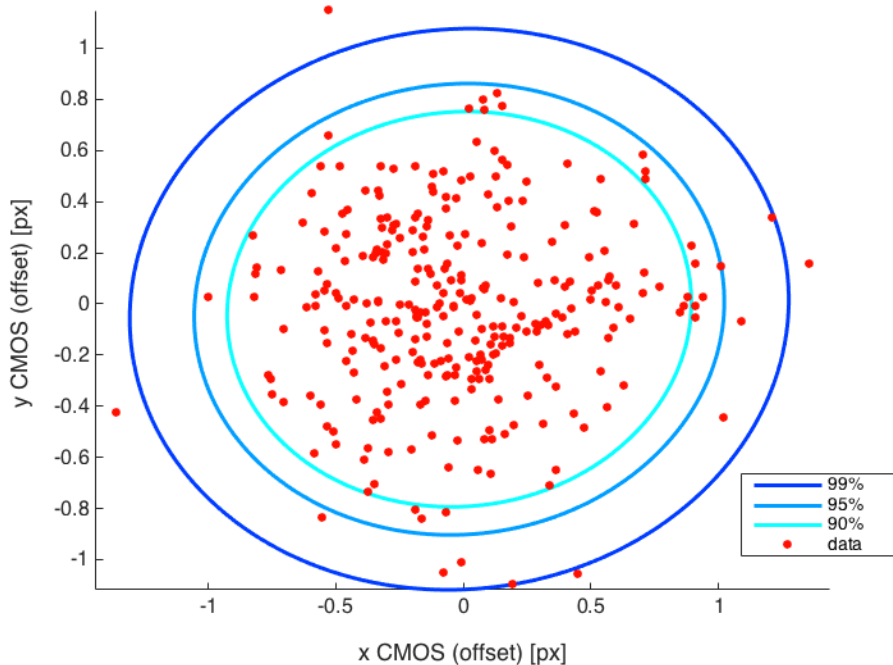


Figure 11. Calibration acquisition results, with 90%, 95% and 99% confidence ellipses.

By analyzing the eigenvectors of the covariance matrix scaled by the square root of the corresponding eigenvalues we can state that there is no evident correlation between the two pixel axes. The 99% confidence ellipse has semi axis lengths of [1.21; 1.14] px. This corresponds to a precision, translated into meters, of [1.69; 1.59]  $\mu\text{m}$  in the x-y directions respectively. In terms of angular displacement, this means an average precision of  $\pm 0.03^\circ$ .

### 3.2 Acquisition strategy and image post-processing

In order to obtain the light spot center, an algorithm was developed to process the CMOS output. The algorithm takes a burst of 50 pictures in 3.5s and averages the acquisitions obtaining a single picture (Figure 12a). The multiple shots are then used to remove the background noise and to detect defects on the surface of the CMOS (such as dust or other debris).

In Figure 12b it is possible to notice how the algorithm is able to remove from the image the presence of some dust particles that were purposely placed on the surface (Figure 12a); in addition, the image is filtered and noise is reduced. This allows to discard any disturbance due, for example, to reflections inside the casing of the sensor: this is a fundamental step in having a correct post processing recognition phase.

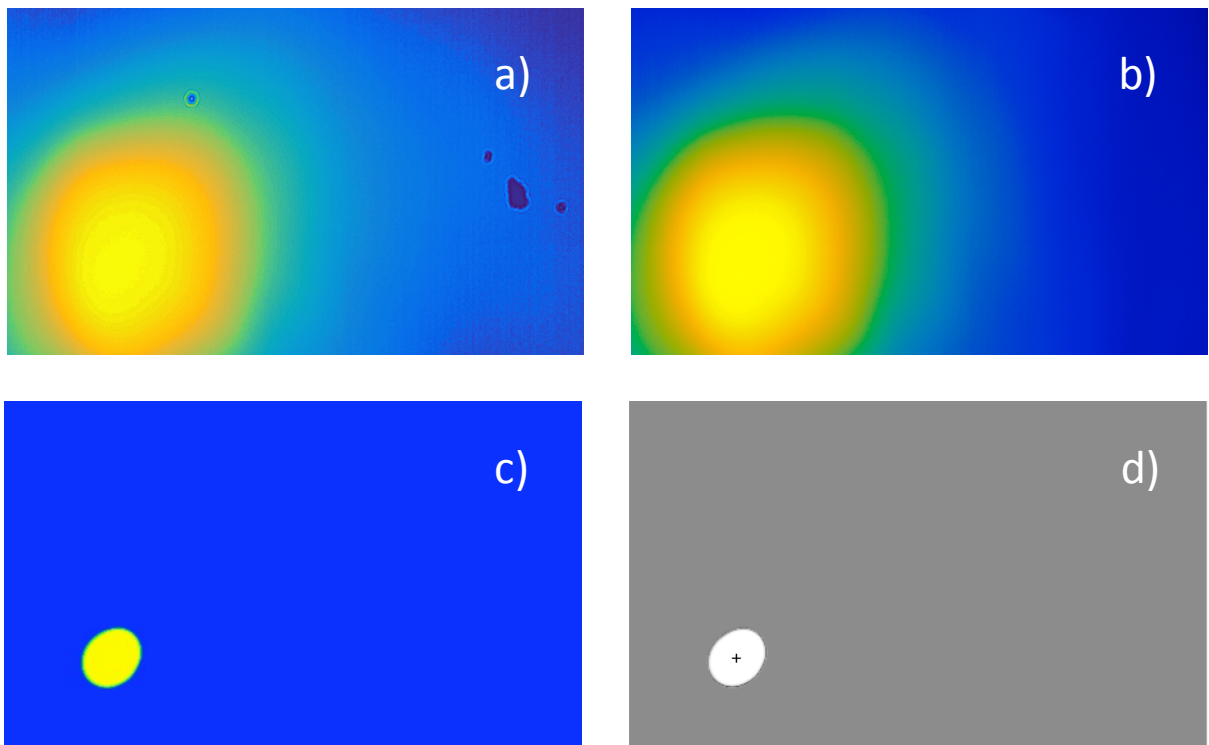


Figure 12. Post processing procedure: original image (a), noise reduction and surface defects elimination (b), thresholding (c) and light-spot center computation (d).

After the noise background removal and the defects correction (operations performed at the beginning of each acquisition), the next part of the processing algorithm computes the center of the projected sunspot. This is done by first converting the acquisition into a gray scale image; then, by setting a custom threshold (which is a function of the camera exposure

settings), the image is further converted into a binary color matrix, resulting in the final projected sunspot ellipse (Figure 12c); the center of this ellipse ( $x_c, y_c$ ) is then computed by simply averaging the  $x_i$  and  $y_i$  coordinates of the ellipse's pixels (Figure 12d):

$$x_c = \frac{\sum_{\text{ellipse}} x_i}{n_x} \quad y_c = \frac{\sum_{\text{ellipse}} y_i}{n_y}$$

### 3.3 Accuracy

In order to estimate accuracy, we performed several tests by exposing the sensor under direct sunlight in clear sky conditions. By knowing the ephemeris of the Sun and by measuring the position and orientation of the sensor with respect to Earth, it was possible to compare the predicted Sun trace with the measured one. We present here a sample acquisition obtained with the device. Total acquisition time is 125 minutes.

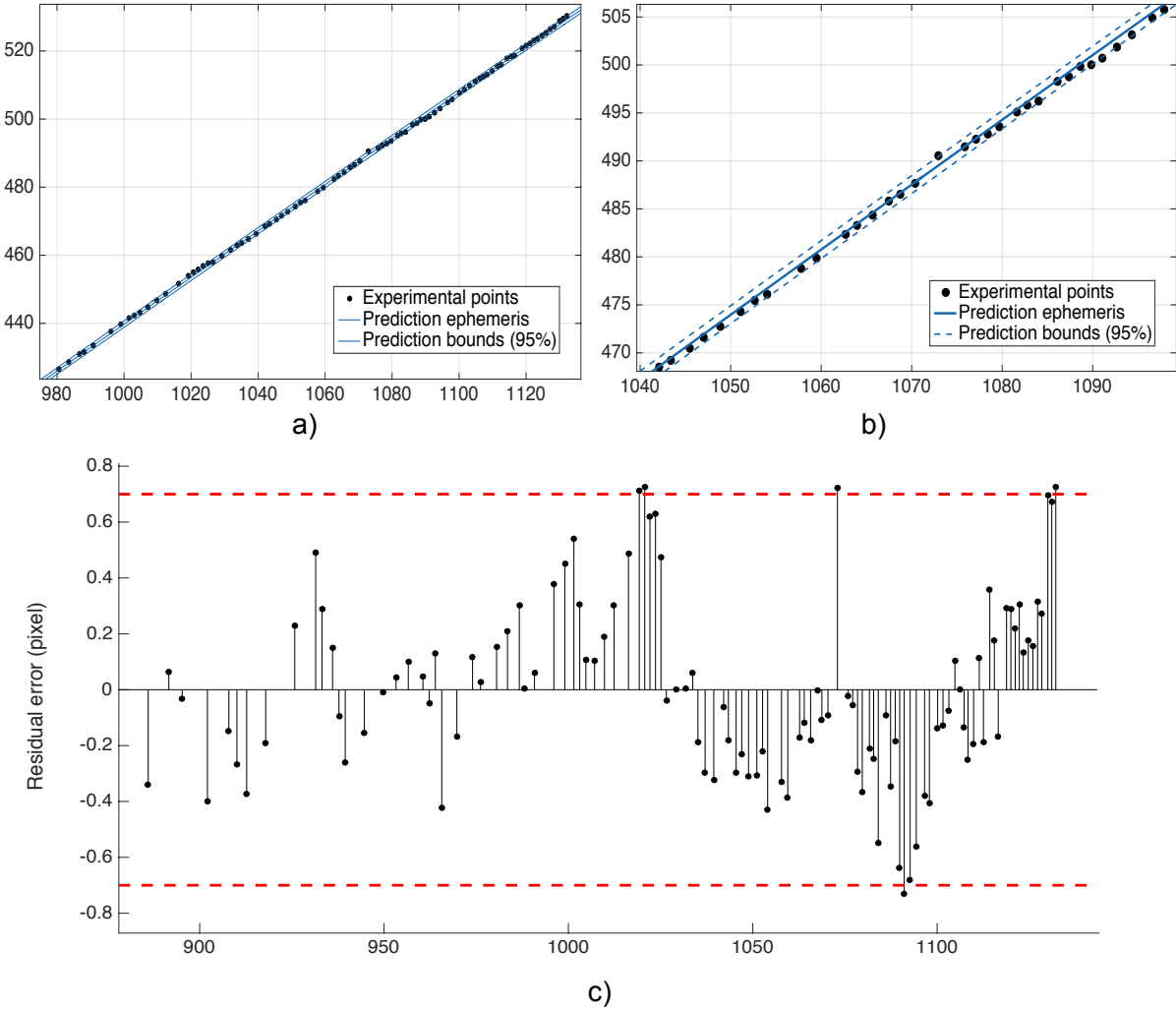


Figure 13. Measured and predicted Sun trace on CMOS (a), zoomed (b). Residual errors plot and 95% bounds (c).

The predicted trajectory can be expressed with a polynomial model which has the following characteristics:

Tab 2: Linear model

Linear model	
$f(x) = p1*x^2 + p2*x + p3$	
Coefficients	95% confidence bounds
p1 = -8.198e-05	(-0.0001021, -6.188e-05)
p2 = 0.8518	(0.8107, 0.8928)
p3 = -330	(-350.9, -309.1)

The experimental data, when fitted with the model, provided the following regression parameters, showing extremely good accordance with the prediction.

Tab 3: Regression parameters

SSE	23.15
R-square	0.9999
Adjusted R-square	0.9999
RMSE	0.4673

It can be seen that the residual orthogonal errors between the projected track and the experimental points are bounded in a  $\pm 0.7$  px band at 95% confidence. This means that experimental accuracy obtainable with the current setup is  $\pm 0.02^\circ$ , provided that the mounting process does not introduce alignment uncertainties and that, if these are present, a calibration procedure with the aid of a known light source is capable of offsetting them.

#### 4 SELF-POWER ASSESSMENT

CMOS technology is demonstrated to consume less power than CCDs, with a further reduction expected with the technology evolution. In fact, it is expected that the already low power requirements of the selected camera (5V, 200 mA) can be reduced in the next years, making it possible to self-power the whole sensor with dedicated solar cells mounted on the pin-hole frame; furthermore, the proposed application does not need high-frequency acquisitions and signal analysis, and the real power consumption is expected to be lower than specified on the datasheet.

Commercial multi-junction solar cells for space applications have reached an efficiency of more than 30%, with a net power production of about  $400 \text{ W/m}^2$  ( $330 \text{ W/m}^2$  at the Sun sensor FOV limits) in Earth orbit; experimental cells reached up to 35% in 2014 [10] and the research is constantly increasing these values. Considering a surface of about  $3 \times 3 \text{ cm}$ , the current technologies can furnish 0.3 W. This result is encouraging, as the aforementioned expected trend of cells efficiency and CMOS power consumption reduction will make it possible to self-power the sensor with commercial cells in about 5-10 years.

## 5 CONCLUSIONS

In this paper a novel sun sensor based on a commercial CMOS camera and a pinhole mask has been presented. The developed prototype showed a Field of View of about  $64^\circ \times 49^\circ$ , with a theoretical resolution up to  $0.026^\circ$ . In order to compare the collected results with the developed models, a complete test campaign has been performed to evaluate the response of the sensor. The laboratory tests showed a predicted accuracy of  $\pm 0.02^\circ$  with a precision of  $\pm 0.03^\circ$  when proper calibration is performed.

Further investigation will focus on the main critical aspects arisen during the prototype development and test. First, other geometries will be evaluated, varying the pinhole diameter and the distance  $h$  between the mask and the CMOS; the calibration testbed will be further improved, introducing a light source with faithful characteristics in terms of irradiance and rays aperture.

Finally, future work will focus on power consumption optimization, evaluating different strategies to reduce the sensor requirements without affecting its performances.

## 9 ACKNOWLEDGMENTS

The authors would like to thank prof. Roberta Bertani and Dr. Claudio Furlan for the kind help in obtaining the scanning electron microscope images.

## 10 REFERENCES

- [1] [http://www.solar-mems.com/smt\\_pdf/commercial\\_brochure\\_SSOC-A.pdf](http://www.solar-mems.com/smt_pdf/commercial_brochure_SSOC-A.pdf)
- [2] Post, M. A., Li, J., and Lee, R., "A Low-Cost Photodiode Sun Sensor for CubeSat and Planetary Microrover," International Journal of Aerospace Engineering, vol. 2013, Article ID 549080, 9 pages, 2013. doi:10.1155/2013/549080
- [3] Ahad, A., and Tanveer, F., "Low-cost design and development of 2-axis digital sun sensor." Journal of Space Technology 1.1 (2011).
- [4] Hales, J., and Pedersen, M., "Two-axis MOEMS sun sensor for pico satellites." Small Satellite Conference (2002).
- [5] Buonocore, M., Grassi M., and Rufino, G., "Aps-based miniature sun sensor for earth observation nanosatellites." Acta Astronautica 56.1 (2005): 139-145. doi:10.1016/j.actaastro.2004.09.006
- [6] Rufino, G., and Grassi, M., "Digital sun sensor multi-spot operation." Sensors 12.12 (2012): 16451-16465.
- [7] Rufino, G., and Grassi, M., "Multi-aperture CMOS sun sensor for microsatellite attitude determination." Sensors 9.6 (2009): 4503-4524.
- [8] Sansone, F., et al. "Low-cost relative navigation sensors for miniature spacecraft and drones." Metrology for Aerospace (MetroAeroSpace), 2015 IEEE (2015): 389-394.
- [9] Sansone, F., Branz, F., Olivieri, L., Francesconi, A.: "Proximity Relative Navigation Sensors For Small-Scale Spacecraft And Drones", 66th IAC, Jerusalem, 12-16 October 2015
- [10] Chiu, P. T., et al. "Direct semiconductor bonded 5J cell for space and terrestrial applications" Photovoltaics, IEEE Journal of 4.1 (2014): 493-497.